CHAPTER 3

The GITO Model System

It was seen in chapter 1 that the results from precession electron diffraction were somewhat mixed in the early precession studies. To really understand what is going on, it is of paramount importance to study the precession method using a model system with known characteristics. In this chapter we investigate precession physics using the Ga-In-Sn-O ternary oxide model system (GITO). The aim of these studies is to understand why precession works in some cases and not in others by closely studying the errors that arise due to the precession operation. The results presented here are reproduced from Own and Marks (2005b) and Own et al. (2005b).

The GITO system was previously investigated as a transparent conducting oxide substrate material for potential use in flat panel displays and solar panels (Edwards et al. 2000; Hwang et al. 2000). The phase studied here, denoted *m*-phase, was first identified using powder X-ray diffraction, solved by a combination of electron diffraction and high-resolution imaging, and later confirmed by neutron diffraction (Sinkler et al. 1998b). Its chemical formula is $(Ga,In)_2SnO_4$. This phase has a monoclinic unit cell with $\mathbf{a} = 11.69$ Å, $\mathbf{b} = 3.17$ Å, $\mathbf{c} = 10.73$ Å, and $\gamma = 99°$. The plane group is p2, and the origin can be defined by fixing the phases of two non-collinear reflections with odd parity. The plate-like structure is shown in figure 3.1.

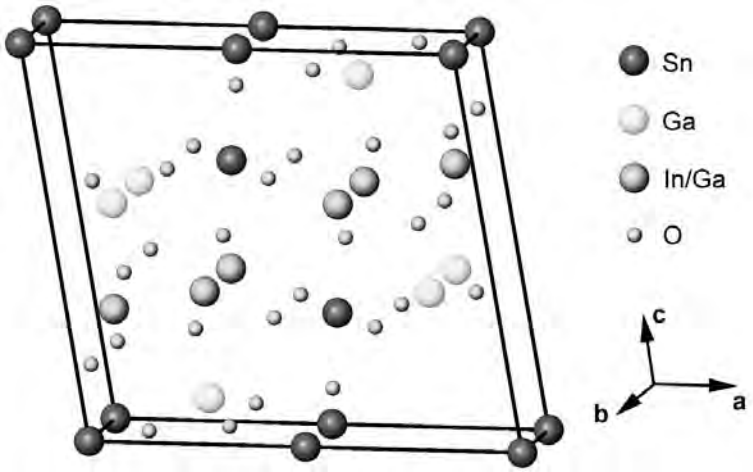

Figure 3.1. Structure of $(Ga,In)_2SnO_4$ (GITO). In/Ga balls represent mixed occupancy sites.

The GITO structure contains relatively heavy elements, making it a strong dynamical scatterer. However, the atomic arrangement projects well in the zone axis investigated here ([010]), so it is a good candidate for probing precession at larger thicknesses. A quick calculation using the relationship

$$R_{overlap} = k \sin \gamma \tag{3.1}$$

where γ is defined by equation 2.5 shows that the FOLZ overlap radius will be 4.14 Å^{-1}. Here, k is the modulus of the electron wavevector (here, 200 kV), $\mathbf{b}^*$ is the reciprocal unit cell distance along the projection axis, and ϕ is the precession semiangle (24 mrad). The small cell distance along the **b**-axis makes the [010] projection particularly suitable for study because the entire measurable dataset is immune to Laue zone overlap (this can be a disadvantage since HOLZ are unavailable for 3D data collection, though 3D data are not needed for the current study). Since the structure is known, there is high confidence in the comparison between simulated data and experiment.

3.1. Rapid *a priori* Solution of a Metal Oxide

A two-dimensional electron precession dataset from GITO was captured on a precession system based upon the JEOL 2000FX microscope described in Own et al. (2005a) and reproduced in appendix C. Operating conditions were as follows: [010] projection; 200kV accelerating voltage; cone semiangle of 24 mrad (0.96 Å^{-1} in the diffraction plane); parallel illumination; 60 Hz precession scan rate; smallest condenser aperture (10 μm); and $\approx$ 50 nm probe size. The dataset (henceforth referred to in this chapter as "precessed") was captured on a GATAN US1000 CCD. A second dataset was acquired by conventional fine probe diffraction (henceforth referred to as "dynamical") using an identical illuminated region and illumination conditions excepting beam precession, and identical probe size and exposure times within experimental error.

Intensity measurements of the digital images were conducted using the EDM crystallography software package (Kilaas et al. 2005). The intensities collected from the datasets were symmetry averaged and used directly with the fs98 code packaged within EDM. The software uses an accurate cross-correlation algorithm similar to that described by Xu et al. (1994) to collect intensities, wherein a unitary spot motif generated by combining reflection profiles is used to quantify the reflection intensities. Details about measurement accuracy are described in appendix F. The precession system was able to bring the diffracted beams down to uniform spots suitable for measurement by this method, and 121 unique intensities were collected in the range of 0-1.4 Å^{-1}. Their values are given in table G.1 in appendix G.

Precession decreases the error between Friedel symmetry equivalents, hence a slight mistilt of the zone axis with respect to the incident beam is tolerable for quantitative electron crystallography. For instance, a mistilt of less than one milliradian is readily compensated by a

precession cone semi-angle of 25 mrad because the effect of shape function geometry is essentially eliminated due to the integration. In more specific terms, the sinc-like functions that describe the excitation are sampled well into their tails where nearly no intensity is contributed (see figure 2.1a), therefore nearly all the available intensity is sampled and the integrated intensities will obey Friedel's law. (A caveat applies if the integration inadequately samples the intensity contained within the relrod, for example, very low $|\mathbf{g}|$ or ϕ is too small).

This effect is seen in the experimental data. Error between Friedel equivalents was evaluated in both precessed and non-precessed diffraction patterns according to the metric,

$$E_{Friedel} = \frac{|F_{\mathbf{g}} - F_{\overline{\mathbf{g}}}|}{2}. \tag{3.2}$$

The non-precessed ZAP was aligned visually to be as on-zone as possible during the diffraction experiment. Datasets were normalized to the strongest reflection to facilitate a direct comparison, and the errors have been plotted in figure 3.2. The precession data had a higher minimum measurement threshold, indicative of more kinematical behavior since the transmitted beam is stronger in relation to scattered beams (note that both datasets had identical exposure times).

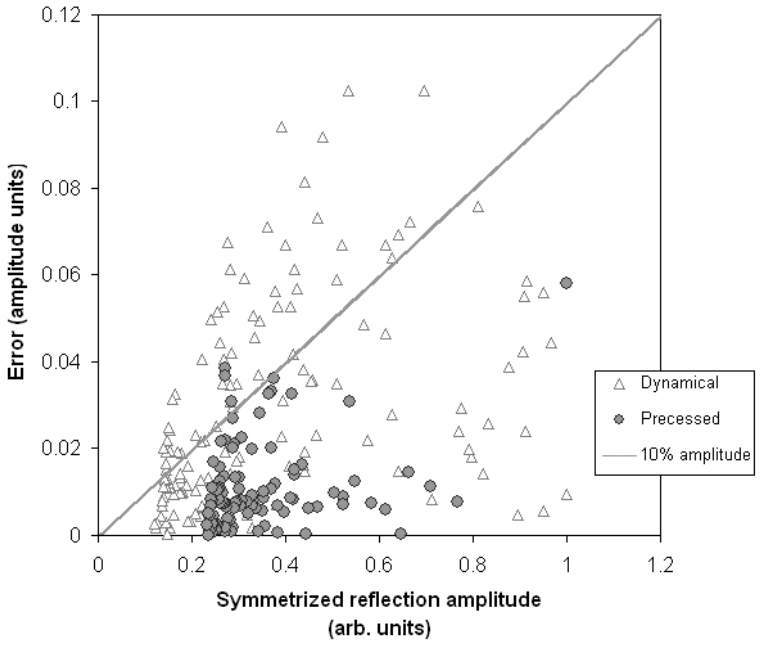

Figure 3.2. Friedel errors (amplitudes). Most precession errors (circles) are less than 10% of the amplitude and decrease with increasing amplitude. Non-precessed Friedel errors have more scatter and often exceed 10% of the measured amplitude due to the asymmetric sampling of relrods.

Figure 3.2 shows that the Friedel error in the precession pattern is overall quite low, and, excepting the strongest reflection, the percentage error decreases as amplitude increases. In contrast, the dynamical dataset errors have larger scatter, and several error points exceed 10% of the reflection amplitude. This is noteworthy because the Friedel error in the dynamical pattern was larger than precession even though spots in the non-precessed dataset were isotropically-shaped and more peak-like, hence easier to measure than the precession pattern which exhibited residual projector distortions that altered spot profiles asymmetrically.

3.1.1. Direct Methods on GITO: Comparison between Dynamical and Precession Diffraction

The set of kinematical amplitudes computed from the known GITO structure will be used as the benchmark for comparison with experimental data. Diffraction patterns from kinematical and experimental PED datasets are shown in figure 3.3. From a qualitative standpoint, it can be seen that key reflections in the experimental precession data with spacings that define the atomic positions (about 0.25Å^{-1} to 1Å^{-1}) match well in relative intensity. The experimental pattern contains increased intensity near the transmitted beam and the outer reflections are damped (figure 3.3(b)), owing to a combination of a Lorentz-type geometric contribution (section 2.1), Debye-Waller type radial damping, and typical dynamical behavior where reflections near strong beams are overemphasized due to strong multiple scattering. The experimental map is especially promising because stronger structural reflections beyond 0.5 Å^{-1}, even though they are damped, still exhibit qualitatively well-correlated intensity ratios.

To better quantify these effects, the experimental dataset amplitudes were plotted against the kinematical amplitudes from the known structure. Figure 3.4 shows experimental precession and dynamical datasets normalized to the strongest intensity in each set. The reflections have been symmetrized by averaging Friedel complements to remove the effects of tilt. Reflection amplitudes are coded by symbol in ranges of $\mathbf{g} = 0.25$ Å^{-1} within the plots. In order for a pseudo-kinematical interpretation to be applicable, the amplitudes must be approximately linear and ratios between reflections should be preserved. The precession data contains several outlier reflections, primarily at $F_{norm}^{kin} \approx 0.2$ (note that this value is specific to the GITO [010] zone axis), and exhibits a distinctive positive offset of weak reflections whose values are above the measurement threshold. Regardless of the offset, most reflections follow the targeted linear trend, and the precession dataset is distinctly linear in comparison to the dynamical amplitudes of figure 3.4(b), which are hopelessly mixed.

Raw GITO precession datasets maintain good linearity to $t \approx 20$ nm according to precession multislice simulations that will be shown later in this chapter. As the thickness increases, intensity deviations manifest first in the reflections outside of the structure-defining reflection range and eventually encroach into the range of reflections that have strong bearing on the structure. This will cause direct methods to generate poorer structure maps. Due to the precession geometry, low-index precessed reflections receive considerable coupled intensity from the transmitted beam, thus the reflections of greatest concern are those nearest the transmitted

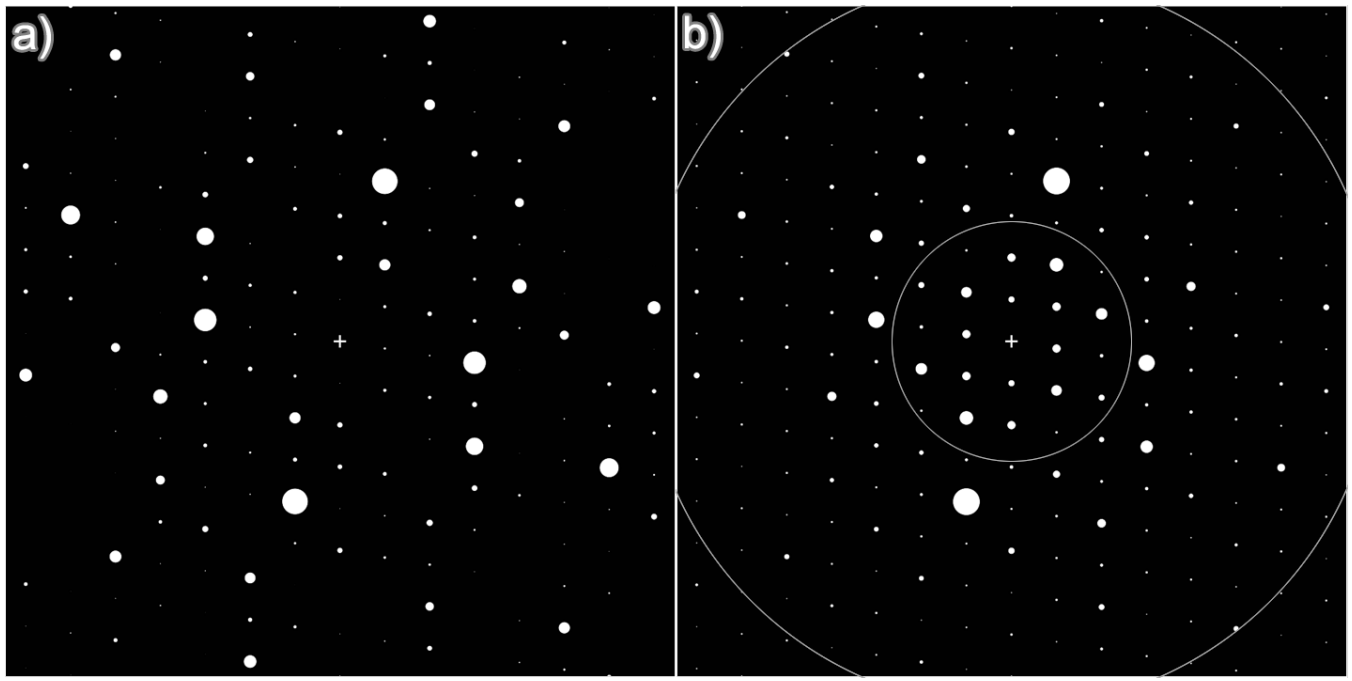

Figure 3.3. (a) Kinematical amplitudes pattern (radius proportional to amplitude) and (b) experimental PED intensity pattern (radius proportional to intensity). The annulus describing the range 0.25-0.75 $Å^{-1}$ is bounded by the circles.

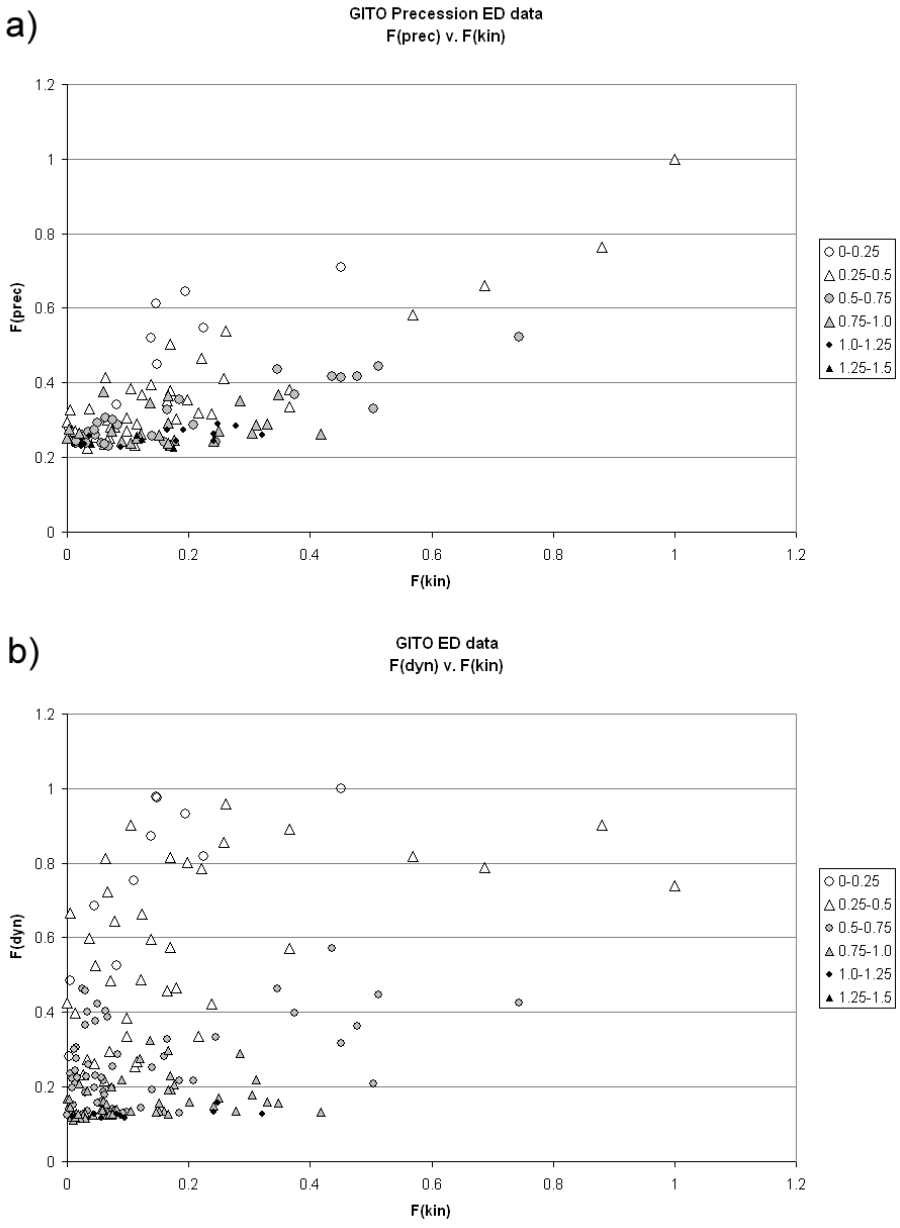

Figure 3.4. (a) Experimental precession amplitudes and (b) dynamical amplitudes plotted against kinematical amplitudes calculated from the known structure. Amplitudes shown are the square root of the measured intensity.

beam that are usually weak for real structures. This behavior suggests that, for unknown structures of moderate thickness, a good starting point is to exclude reflections that fall outside of the structure-defining range of 0.25 $\text{Å}^{-1} < \mathbf{g} < 1.25$ Å^{-1}. This approach is effective with precession data from GITO crystals to about $t = 750$ Å when a 24 mrad precession semi-angle is used. Higher precession semi-angles can improve this to some extent (extending the range by 5-10 nm) but HOLZ overlap with the ZOLZ is likely. Larger thicknesses will certainly require a forward calculation to correct the intensities for multiple scattering; one such approach is the two-beam correction employed in the earlier study by Gjønnes (Gjønnes et al. 1998b). The conditions for when this is necessary are established in later sections of this chapter.

The precession amplitudes with $\mathbf{g} < 0.25$ Å^{-1} excluded were employed in a direct methods calculation and produced four unique solutions (shown in figure 3.5(a)). The solution with the clearest peak-like features from the dynamical dataset is given in figure 3.5(c) for comparison. The precession solutions bear near-identical features to each other and demonstrate well-defined peak locations. Some of the strong scatterers in the structure are weakly emphasized (i.e., the In/Ga columns at 0.35**a**,0.38**c**, see figure 3.1). However, all expected atom locations contain atom-like features above the noise floor that would be considered as potential atom locations in an *a priori* structure investigation. The quality of these solutions, compared with the solution from the dynamical dataset acquired from the identical specimen region, is unmistakable.

Figure 3.5(c) is typical of a first-try solution with a complex oxide of unknown thickness. The quality is not as good as the precession solutions; it is well-known that bulk oxide structures are as a rule very difficult to solve from TED data alone. In stark contrast to precession, the best dynamical solution only located Sn atoms at the corners and middle of the unit cell, and the central atoms were placed at incorrect positions. Of seven unique solutions generated from the dynamical data, only two possessed atom-like features. Neither of the solution maps would be trustworthy unless more *a priori* information was available to constrain the calculation such as phases from high resolution imaging.

In addition to generating excellent starting structures, some favorable effects of thickness insensitivity are also seen in the PED data. Thickness fringes were present in the image of the illuminated region, indicating that the crystal was wedge-shaped. As was described in section 1.4, aspects of the structure such as the oxygen columns or heavy cation columns (manifesting as sharp well-defined features) exchange prominence in the exit wavefunction with increasing crystal thickness. This is due to differing oscillation periodicities with thickness for atomic columns of differing composition. To get projections that faithfully indicate all features of one type (critical for direct interpretability), thin and uniform crystals are required to avoid overlap of oscillations from multiple thicknesses of the same column type.

In the case of GITO, the Babinet solutions generate peak-like features only at anion columns, arising from slow variation of channeled intensity within oxygen 1s states (Sinkler and Marks 1999b). Simulated images show that interpretability of the Babinet rapidly diminishes beyond about 30 nm thickness. The poor quality of the dynamical solution in figure 3.5(c) suggests that the specimen must be thicker than 30 nm and/or contributions from multiple thicknesses

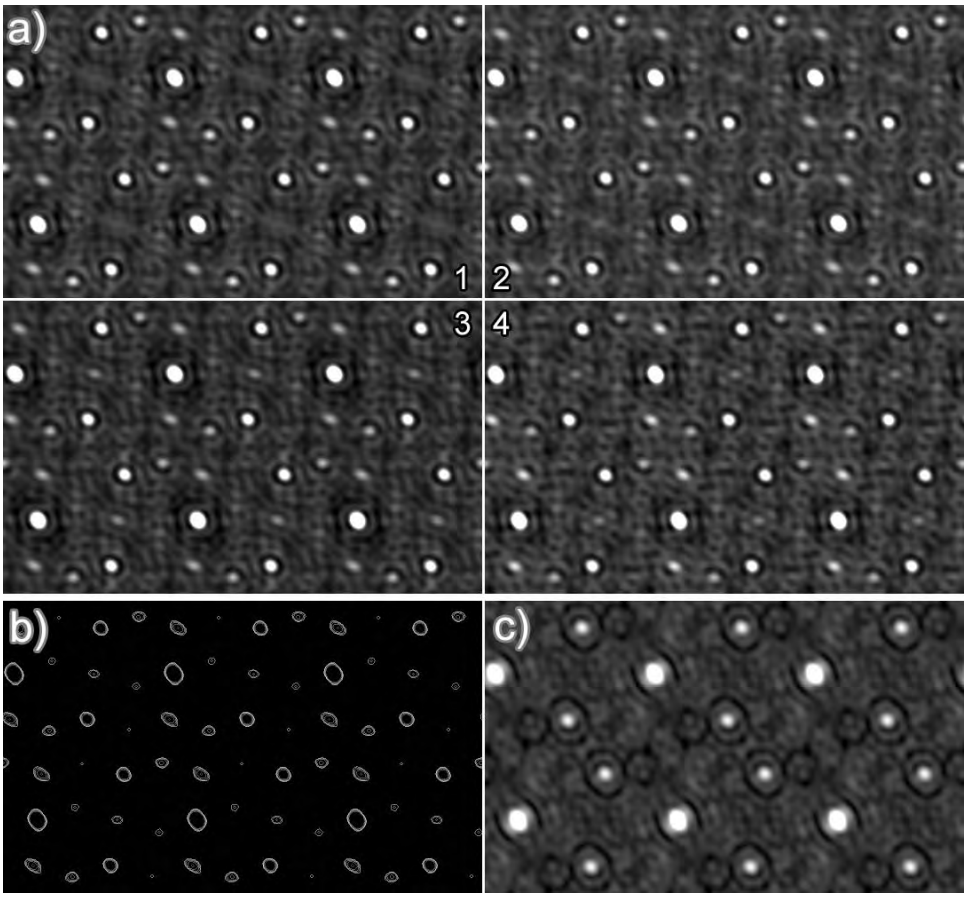

Figure 3.5. a) Four unique DM solutions generated from precession amplitudes. Reflections below $\mathbf{g} = 0.25$ Å^{-1} were excluded. b) Topographical map of solution 4. Well-defined peaks above the noise floor correspond to atomic positions. c) DM solution from dynamical dataset. No high resolution phases were used to generate these maps.

are destroying the intensity relationships that generate correct phases. In contrast, not only were realistic solutions extracted by PED from a specimen that was thicker than 30 nm and wedge-shaped, peak-like features were readily recovered at the *cation* locations showing that the solution results from pseudo-kinematical direct methods rather than dynamical direct methods. In other words, intensity relationships are preserved regardless of thickness variation. From this result, it can be concluded that PED of moderately thick crystals ($<$ 50 nm) with good projection characteristics requires no additional phase information to restore structure maps of the kinematical scatterers.

It has been suggested by Dorset and others to increase contrast of the electron diffraction data by using intensities with direct methods rather than structure factor amplitudes (Dorset 1995; Gemmi et al. 2003; Weirich 2004). As discussed in section 1.4, this approach is supported

by a two-beam argument applicable to polycrystal diffraction, texture patterns, and possibly also to precession data (effective integrated two-beam). From Blackman theory (Blackman 1939), the measured intensity $I_{\mathbf{g}}$ is related to the kinematical structure factor $F_{\mathbf{g}}$ as

$$I_{\mathbf{g}}^{dyn} \approx F(\mathbf{g})^{\alpha}, \tag{3.3}$$

where the exponent α varies from 2 to 1 as the product of thickness t and $F(\mathbf{g})$ increases (equations 1.26 and 1.27). In the limit of PED on thicker crystals where the structure is unknown, use of intensities approximates a dynamical two-beam correction that can be used to generate starting structure maps. This is supported by the intensity diffraction pattern of in figure 3.3(b), which matches the kinematical amplitude pattern of 3.3(a) well. The practical effect of using intensities is a preferential enhancement of strong beams which, if the strong structure-defining amplitudes are nearly correct with respect to each other, emphasizes key structural features above "noisy" weak reflections that can generate ambiguous oscillation maxima in the Fourier synthesis.

Incorporating this alternate approach with the GITO data, the strong structure-defining reflections in the 0.25 Å - 0.5 Å region become more prominent as the contrast between strong and weak beams is enhanced. The resulting map (figure 3.6(a)-(b), where all measured reflections were included in the direct methods) more clearly shows atom-like features at all expected cation locations due to attenuation of noisy reflections. Peak locations from the intensities-derived map are consistent within a few picometers to those found by using amplitudes with low-$\mathbf{g}$ reflections excluded (figure 3.5).

The question arises as to why both the amplitudes (excluding low-$\mathbf{g}$ outliers) and intensities (all reflections) generate good solutions with atom positions coinciding perfectly. Recalling equations 1.26 and 1.27 that describe the limits of the Blackman equation, the answer lies in the fact that intensity ranking relationships are preserved in both cases so they will likely yield similar phase relationships. In the intensities case, the value of structure-defining reflections are much stronger than weaker reflections, so atom-like features are sharper, however this will only be be applicable in the limit of large thickness ($A_{\mathbf{g}}$ large).

The cation positions measured from the amplitudes-derived map (unrefined) are given in table 3.1. HREM and neutron-refined GITO atom positions from Sinkler et al. (1998b) are reproduced for comparison, showing good correspondence with precession results. Precession-derived maps without subsequent refinement result in column positions located on average within 4 picometers of the neutron-refined positions.

3.1.2. Discussion

In this section, electron precession has demonstrated the ability to linearize the GITO dataset to a kinematical approximation allowing nearly-direct interpretation. The experimental precession data from GITO is linear in the regime where the structurally important reflections are located, and appears to be much less sensitive to the variations in thickness that prove debilitating for

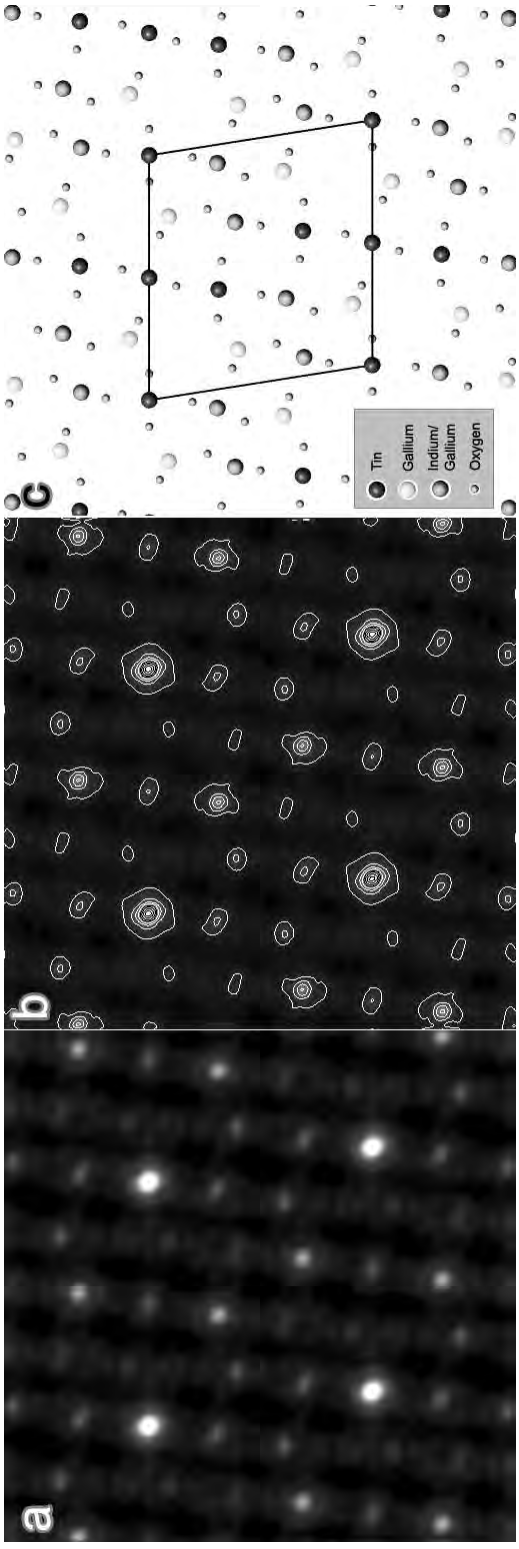

Figure 3.6. DM solution from precession intensities (all reflections included).

Table 3.1. GITO atom positions from HREM, neutron diffraction (refined), and unrefined positions from precession. Atom positions from PED match very closely with the neutron-refined positions.

	HREM		**Neutron**		**Precession**		Displacement (Å)	
	x	z	x	z	x	z	ΔR_{HREM}	$\Delta R_{neutron}$
Sn1	0.0	0.0	0.0	0.0	0.0	0.0	0.0	0.0
Sn2	0.515	0.062	0.5	0.0	0.5	0.0	0.474615	0.0
Sn3	0.594	0.320	0.5918(6)	0.3112(7)	0.585113	0.312169	0.017950	0.0065(5)
In/Ga1	0.305	0.360	0.3281(6)	0.3859(7)	0.345947	0.379929	0.275989	0.0516(5)
In/Ga2	0.078	0.328	0.0756(8)	0.3053(9)	0.079877	0.305699	0.057683	0.0023(7)
Ga1	0.172	0.672	0.1500(5)	0.6022(6)	0.172498	0.602720	0.552591	0.0684(8)
Ga2	0.234	0.031	0.2624(5)	0.0869(5)	0.232436	0.078043	0.255026	0.1217(5)

conventional electron diffraction datasets. The results also suggest a systematic behavior to the data errors present. Exclusion of overemphasized reflections in precession datasets that have little bearing on the structure is a suitable starting strategy, and a second strategy in the limit of large thickness is to use intensities.

A comprehensive understanding of these errors in relation to thickness and illumination conditions is now necessary to allow use of precession data in a general pseudo-kinematical capacity. It is encouraging that precession data, from experimental conditions that would ordinarily be very difficult for generating useful starting structures, has been directly usable with little to no modification, and without phase information. In the next section, we will use simulation to understand why this is so.

3.2. Precession Simulation

The n-beam calculations by Gjønnes et al. (1998b) on Al_mFe were made along the azimuthal precession circuit θ within 0.5° of the Bragg condition for each reflection and were reported to converge using a small number of beams within an aperture radius of 1 $Å^{-1}$ (roughly 20 beams, varying in quantity and selection with Bragg reflection along the circuit). Details of which beams were used, how they were chosen, and the resolution of the calculation were unfortunately never published. No other precession data simulations have been reported thus far, so a comprehensive benchmark of experimental precession results does not yet exist in the literature. While the details are not available, it is nevertheless evident that the problem space in the previous study was sampled somewhat sparsely. Here, full dynamical multislice calculations will be used to establish a robust baseline for comparison with the experimental data from GITO.

Precession datasets for the [010] projection of GITO were simulated using the NUMIS multislice code for a wide range of thicknesses at 200 kV with parallel illumination. The netron-refined atom positions from table 3.1 were used in the simulations, and Debye-Waller factors of 0.3 Åand 0.5 Åwere used for the cations and oxygen atoms, repectively. Individual tilt events were calculated along the azimuthal circuit (increasing ϕ as in figure 1.10) and integrated into a unified dataset. The granularity of the simulation will be referred to as "angular resolution" and corresponds to $\frac{360^o}{N_t}$ with units of degrees, where N_t is the number of discrete tilts. Since tilt inherently enhances intensity loss from the edges of the matrix used in the multislice calculation, care was taken to prevent loss of intensity during propagation through the crystal that might skew the exit wave amplitude. First, the phase grating was expanded in dimension such that greater than 99.5% of incident intensity was retained for all simulations to 160 nm (1000 slices). Second, calculations were set to include beams to a very high resolution of about 7.5 $Å^{-1}$ to ensure re-diffraction from high-angle beams back into the central beams was fully accounted for. For comparison, un-precessed datasets using zero tilt ("dynamical" datasets) were also calculated for identical thicknesses using the same simulation settings. The simulation output included reflections to 1.5 $Å^{-1}$ which is just beyond the measurement limit for most experimental datasets.

An analysis of intensity integration convergence was conducted to confirm reliability of the tilt summation approach. Several precession simulations were conducted on the GITO system with integrated intensities normalized to the transmitted beam. Convergence for small thickness was first to be evaluated. Convergence was rapid, occurring with 8 discrete tilt samples for 4 nm specimens, and 32 tilts for 16 nm. At larger thickness, it was found that much higher resolution was necessary for convergence: substantial errors appeared by $t = 50$ nm for $\phi = 24$ mrad and the errors were exacerbated when larger cone semi-angle was used (in the worst case up to 20% error in strong beams is seen). The strong dynamical mixing in thick specimens combined with the rapid integration of higher-index relrods at large precession angle necessitated finer sampling. For this reason 0.36° angular resolution (1000 discrete tilts) was used for all simulations in this study.

Figure 3.7 confirms that precession multislice correctly describes the data. The thickness of 412 Å, to be derived from the experimental data in the last section of this chapter, demonstrates good agreement within experimental error. This is in part due to PED's insensitivity to the thickness variation, further evident from the regression analysis of un-precessed experimental data (not shown) which yielded a much lower $R^2 \approx 0.45$.

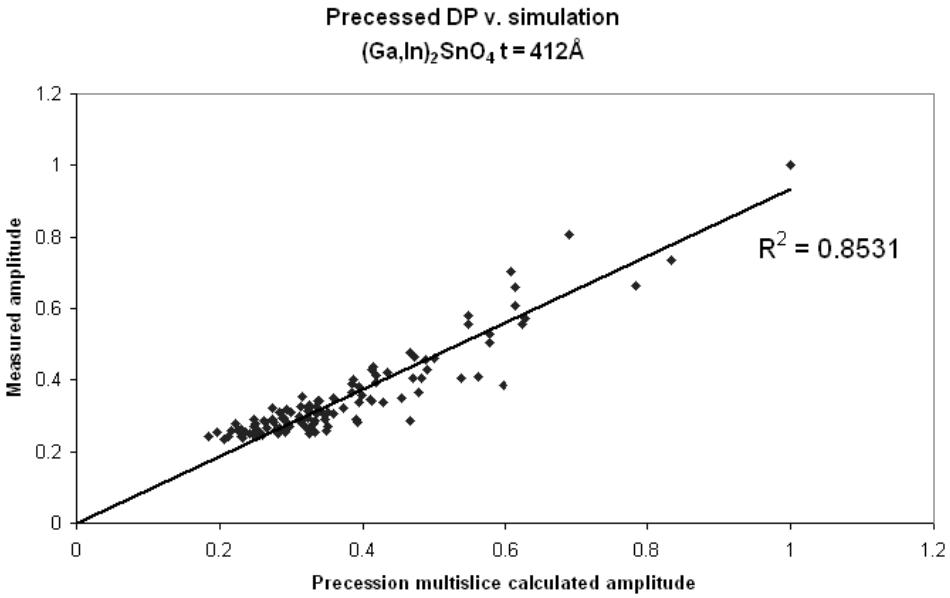

Figure 3.7. Precession amplitudes (normalized) plotted against amplitudes calculated by precession multislice.

3.2.1. Amplitude Reference Plots

Plotting experimental data against the kinematical reference is a useful metric for gauging how well a dataset will solve, previously demonstrated by the amplitude plots of 3.4. This will now be extended through multislice simulation to efficiently explore a large portion of experiment space.

Since beam intensities often span several orders of magnitude and strong beams are substantially more intense than most beams in the set, the data are easier to interpret if amplitudes (normalized to the strongest beam) are plotted. In the ideal case, the two axes will have a one-to-one correspondence. However, as long as a roughly linear relationship is preserved, favorable solutions will still be generated, even with errors of 10-20% in the strong reflections. Weak intensities that have received extra scattering intensity due to dynamical effects — in effect weak beams converted into strong beams — are the most detrimental to the success of direct methods. They are a frequent feature of dynamical datasets such as the dynamical GITO dataset from figures 3.3(b) and 3.4(b).

A montage of reference plots of multislice precession data is given in figure 3.8 demonstrating trends over thickness t and cone semi-angle ϕ. The montage is divided into three dataset groups:

(1) The top row of plots is the un-precessed case (dynamical).
(2) The left column shows the behavior for a very thin specimen (4nm).
(3) The 16 plots in the lower right show the effect of increasing precession angle for a variety of specimen thicknesses.

The precession angle ϕ of 10, 24, 50, and 75 mrad corresponds to reciprocal distances (in Å^{-1}) of 0.398, 0.956, 1.99, and 2.99, respectively, at 200 kV. The following table establishes some simple terminology for describing the relevant thickness regimes:

Table 3.2. Terminology for thickness ranges.

thickness range	descriptor
0-25 nm	small
25-50 nm	moderate
50-100 nm	large
100+ nm	'very large'

A qualitative analysis of the multislice data reveals interesting global behaviors. As would be expected, the data become less kinematical with increasing t regardless of precession angle. A clear improvement can be seen in the small-to-moderate range of thicknesses as ϕ increases.

Looking first at the smallest thickness of 4 nm (at the practical limit of sample preparation methods), at $\phi = 0$ mrad demonstrates some scatter and already the strongest reflection has over 1000% error (the reflection at $F^{kin}_{norm} \approx 0.25$). Introducing a small precession angle of 10 mrad improves the linearity of datasets and in the plots for small thickness crystals one can readily track the errant reflections migrating toward the kinematical reference line described

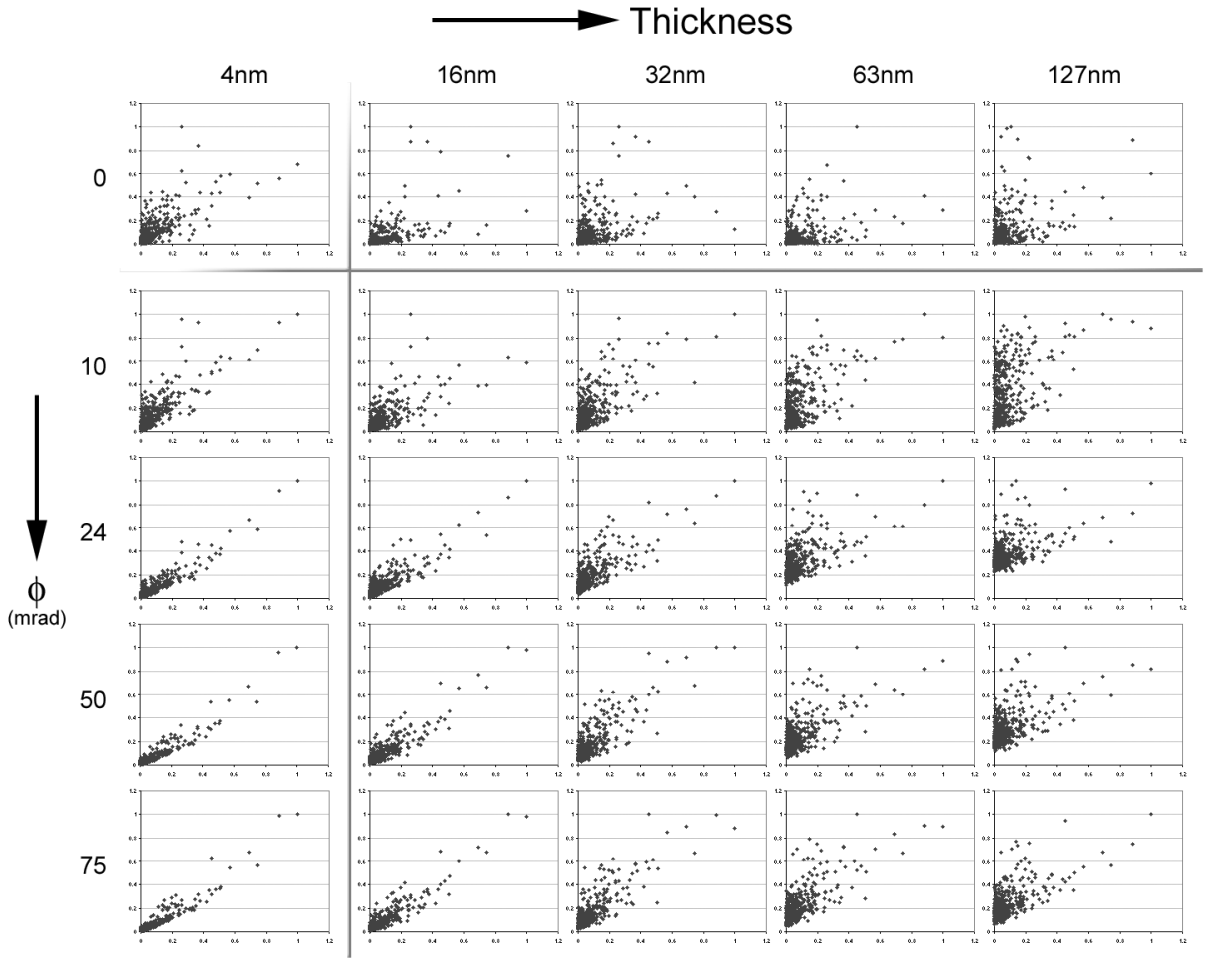

Figure 3.8. Montage of amplitude reference plots for GITO. In each plot, the abscissa represents kinematical amplitudes and calculated amplitudes are plotted along the ordinate. The plots are arranged in order of increasing thickness and angle as indicated.

by $F^{prec}_{norm} = F^{kin}_{norm}$. Moving to 24 mrad, datasets from thin specimens become even more kinematical, and accompanying additional increase of ϕ the weak reflections improve further.

Unfortunately the improvements break down when t is large, and a marked positive error in the weaker reflections is seen in all datasets for large thickness. This condition will require corrections which will be discussed in chapter 4. Nevertheless, the precession datasets at high angle will indeed be more amenable to Direct Methods than the dynamical dataset; for example the 127 nm PED data behaves quite similarly to the 63 nm PED data, and both would yield better structure maps than most un-precessed diffraction experiments excepting the thinnest geometries. The intensities have similar aggregate behavior over a range of thicknesses, implying a systematic character to the errors.

The plots in figure 3.8 indicate PED data can be used directly with structure solution codes with no modification up to moderate thickness (at least 30 nm). Positive error in the weak reflections primarily occurs in the low index reflections and is due to the sampling geometry; as shown in the previous section, the most errant reflections cluster near the transmitted beam because the excitation error for low index reflections is small (corresponding to slow sampling of the relrods) and in precession, systematic dynamical effects are limited to low g by the Laue circle. These errant reflections can be excluded because they are not structure-defining reflections. In the regime of moderate-to-large specimen thickness (40-70 nm), however, the errors encroach into the structurally important reflections and will require more sophisticated correction measures.

3.2.2. Amplitude Error Analysis

A more thorough understanding of what is going on is afforded by examining the errors quantitatively. The deterioration of linearity between precession intensities and the kinematical reference as t increases manifests mostly in the low-g reflections. With increasing crystal thickness, the positive error of weak reflections becomes larger from geometry: since in reciprocal space the periodicity of oscillation within the sinc-like relrods is reduced (refer to figure 2.1), reflections near the transmitted beam are sampled less rapidly and therefore more intensity is integrated than higher-g reflections. A second source of error arises from dynamical effects: because dynamical effects are most prevalent near the transmitted beam (both systematic and non-systematic dynamical scattering), low-g reflections receive considerable dynamical scattering intensity. By 63 nm there is already substantial scatter in the datasets due to this phenomenon.

Realistically, to use PED data without modification, small-to-moderate thickness specimens are needed. This is a marked improvement from the conventional dynamical case: in the case of GITO, the range of experimental thicknesses that yield directly-interpretable pseudo-kinematical data (specifically yielding cation positions) is extended by about a factor of ten from a few nanometers to at least several dozen nanometers. The thickness range for which DM would be effective will predictably decrease for structures that project poorly or contain heavier

atoms, and increase for materials that contain lighter atoms that project well but scatter less strongly. Examples of this can be seen in chapter 5.

A better understanding of precession in the GITO system is afforded by examining error surfaces plotted with respect to $|\mathbf{g}|$ and thickness t (Figure 3.9). These 'lobster tail' plots

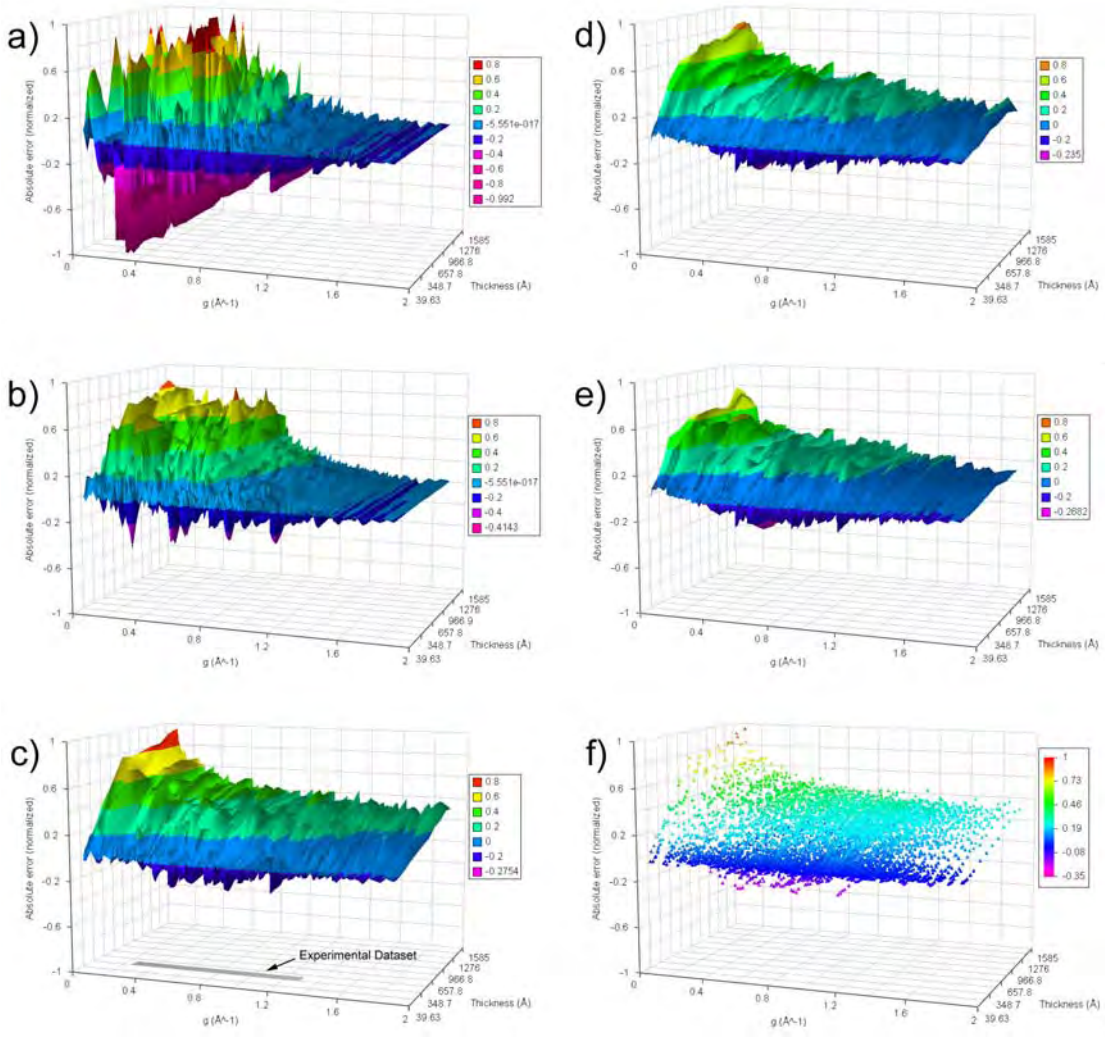

Figure 3.9. 3-D surface plots of absolute amplitude error ($F_{\mathbf{g}}^{exp} - F_{\mathbf{g}}^{kin}$) against $|\mathbf{g}|$ and thickness. (a) Dynamical (non-precessed) dataset errors showing particularly large error spread within structure-defining reflections $g \subset [0.25, 1]$. (b)-(e) Precession dataset errors for ϕ = 10, 24, 50, and 75 mrad respectively. Experimental dataset parameters are indicated in plot (c). (f) Scatter plot for 24 mrad showing that for realistic specimen thicknesses (< 50 nm) almost all errors fall within the range [-0.2, 0.4].

represent absolute deviations from kinematical of the normalized precession multislice datasets ($E_{norm} = F_{\mathbf{g}}^{exp} - F_{\mathbf{g}}^{kin}$) and give a wide view of experiment space within a single plot. Absolute errors are employed because the reflections of most interest are the strong ones (the ones that define phase relationships for other beams). Large errors correspond to intensities that should be weak and become strong due to excitation of alternate scattering paths or vice versa. Generally, low error throughout the dataset is desired, but special attention should be given to the structure-defining reflections that lie within the range 0.25-1.0 Å^{-1}. Strong reflections in this range are most important for the success of structure solution codes, and if errors in this regime are circumvented the dataset becomes more tractable.

It is important to recognize that tolerable errors correspond to about 10-20% intensity error for strong reflections ($\approx 40\%$ peak amplitude error). Errors in figure 3.9 are differentiated graphically by dividing the error regime into blocks corresponding to 20% amplitude error. The regime of most interest is the band corresponding to error = ± 0.4 (blue/dark blue). Note that while neighboring $|\mathbf{g}|$ do not have an intrinsic relationship with each other unless they are related within systematic rows, the data have been presented as continuous surfaces to better illustrate oscillatory behavior in the error map. The bumpiness of the surface, a result of the sharpness of oscillations between neighboring $\mathbf{g}$, is a crude but effective estimator of the amount of dynamical scattering occurring within the system.

Figure 3.9(a) is the error surface for the conventional diffraction dataset plotted with respect to $\mathbf{g}$ and t. The error values reflect the classic damping effect where reflections near the transmitted beam are strong and their amplitudes decay with $\mathbf{g}$ (e.g., when intensities are large, their errors will likely be large as well). For small t, there is substantial error beyond the $\pm 40\%$ range indicating strong dynamical effects. Oscillations are relatively high in amplitude, though most errors are on the order of about 0.2-0.4. The important structure-defining reflections are the most adversely affected, with amplitude errors as high as ≈ 0.6, and demonstrate rapid oscillatory behavior with t. The thick crystal regime demonstrates very dynamical characteristics and the largest errors are tens of thousands of percent occurring in the band of critical structural reflections.

PED at 10 mrad reduces positive errors to < 0.8 and the error surface is flattened. More notably most negative errors are eliminated (figure 3.9(b)). Gaussian radial damping is still present for all thicknesses, and 10 mrad is still quite dynamical even for small thickness where dynamical effects should be lowest, in accordance with the 10 mrad plots in figure 3.8. Increasing the angle to 24 mrad enhances the flattening effect considerably, and the error for thin crystals is greatly diminished (figure 3.9(c)). As t increases, the errors grow, especially for low $\mathbf{g}$ due to accentuated systematic dynamical effects occurring near the transmitted beam. The peak error occurs for the largest thickness (160 nm) near the transmitted beam. Large precession semi-angle (3.9(d)-(e)) decreases the overall error, and additionally flattens the low-thickness region quite like a serrated knife-edge such that intensities remain kinematical for larger t ($\approx$ 5 nm more for each 25 mrad step in angle). Figure 3.9(f) is a scatter plot for $\alpha = 24$ mrad

that shows that the error surface is thin (low oscillation) and is sharply tilted up toward small **g** and very large t. This is common for all precession datasets above 20 mrad.

The experimental parameter space where directly interpretable data will be available corresponds to reflections that have low aggregate error ($t < 50$ nm). This is an extremely useful range because it is easy to make real specimens (both powder and single crystal) within this dimension. As thickness increases, the positive offset of low-**g** reflections creeps into the structure-defining reflections as seen in the experimental data, necessitating corrective measures.

The results from this section are best summarized as a list of features:

(1) Precession flattens the error surface (thickness oscillations are dramatically reduced).
(2) Errors manifest as a positive offset in reflections near the transmitted beam and are exacerbated with increasing thickness.
(3) Higher precession angle further enhances the error-flattening property and reduces the near-transmitted errors.
(4) Higher angle can convert intensities at low **g** and small-to-moderate thickness into nearly-kinematical intensities.
(5) The above statement is not without limit - increasing angle yields diminishing returns and too high of an angle results in FOLZ overlap.
(6) Dynamical data exhibit Gaussian radial damping on the **g** axis whereas precession distributes errors over the band.
(7) PED data, bandlimited to include only structure-defining reflections, are nearly kinematical.
(8) The flattening effect is limited: corrections will be necessary for large thickness.

3.3. R-factor analysis

Until now, the discussion has centered around recovering a starting structure model. Refinements, while very successful for surfaces, may be difficult for bulk structures if the data is confounded by contributions from multiple thicknesses. In simple terms, the success of structure refinements depends upon reliably locating global minima in the error metric. The solution space for bulk structures is enormous because not only are the spatial positions variables, the thickness varies as well and is a poorly conditioned variable (e.g., a relatively small change in thickness generate large changes in the dataset). In conventional diffraction and imaging studies of bulk structures, rapid intensity oscillation with thickness often increases errors across the dataset that either obscure the global minimum and/or create multiple minima.

It is relevant to mention the case of surface reconstructions in some detail, because refinement is often straightforward. It is known that thickness is very small so kinematical methods can often be employed where thickness is not a variable. If multislice refinement is used, the solution space to be probed is minimal because possible atom positions are usually confined due to planarity. In relation to conditioning of the thickness variable, recall that precession is less sensitive to thickness in general, evidenced qualitatively in the surface plots of figure 3.9. Bulk

refinement will benefit considerably if thickness becomes a better-conditioned variable through thickness insensitivity.

In the previous section, application of DM to precession data has recovered the atom locations to within 4 picometers of the known GITO structure on average. This is essentially the correct structure, therefore, precession multislice can be compared directly with the experimental data from GITO to study the effect of thickness in PED.

R-factors (see equations 1.17 and 1.18) have been calculated for the experimental datasets (both precessed and non-precessed) against the simulated crystal thicknesses. The same atom positions and Debye-Waller factors from section 3.2 were used in the simulations, and thickness was the only parameter that was varied. A 24 mrad cone semi-angle was used for the precession simulations. Values for R_1 are plotted in figure 3.10(a), with the region around the expected thickness sampled more finely than elsewhere. The precession R-factor demonstrates a clear global minimum that spans a relatively broad range of thicknesses (30-45 nm) and the lowest value ($R_1 = 11.78\%$, 121 symmetrized reflections measured) corresponds to a thickness of 41.2 nm. A plot of experimental amplitudes v. simulated amplitudes for this case is shown in figure 3.7. The relatively flat minimum supports the observation of thickness insensitivity because a contiguous range of t matches the experimental precession data well.

The precession R_1 values within the vicinity of the minimum are exceedingly low compared to the dynamical experiment, which oscillates with only one clear minimum (best $R_1 = 43.98\%$

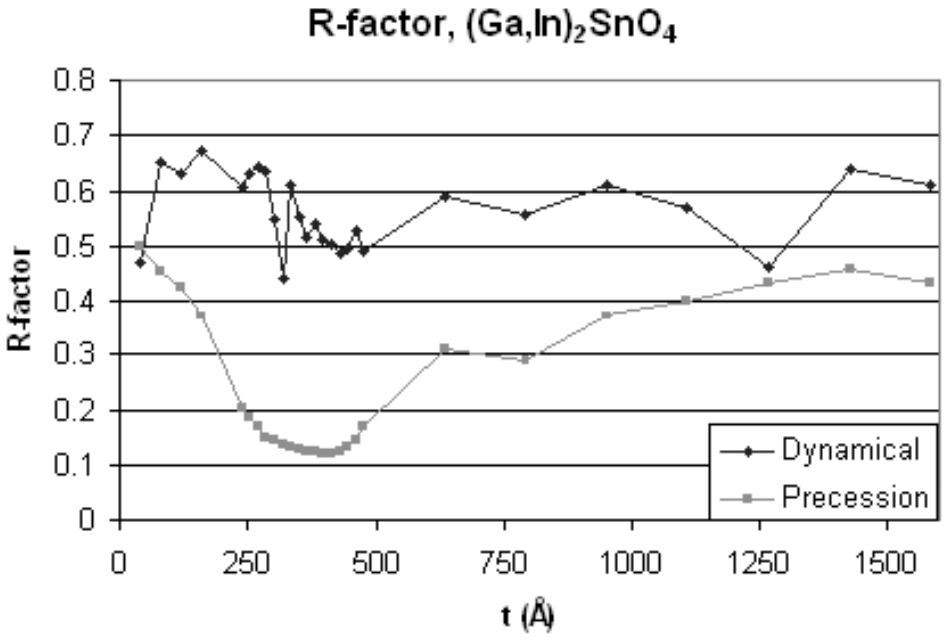

Figure 3.10. R_1 for the GITO experimental datasets. Precession datasets have a clear global minimum and indicating a nominal thickness of $\approx$ 40 nm.

at 31.7 nm, 172 reflections; note this is not a refined R_1). Additionally, the unrefined precession R_1 is much lower than those found in conventional electron crystallography refinements. For comparison unweighted R_2 (calculated using intensities, equation 1.18) for precession is 23.6% matching the same thickness of 41.2 nm. R_2 is naturally higher because most intensities are very small in value compared to the strong beams and because it is unweighted all intensities are treated equally (small intensities in the denominator dominate the sum).

Detail plots are shown in figure 3.11 for both experimental datasets illustrating the parameter space they occupy. The critical observation is that with precession, the experimental parameters yield low absolute error and additionally maintain the same character with increasing thickness. With reflections $\mathbf{g} < 0.25$ Å^{-1} excluded, the integrated precession intensities naturally correspond quite well with the kinematical intensities.

3.4. Summary

In this chapter PED on the GITO system has been investigated in detail from the perspective of empirical results and also through simulation. An experimental dataset obtained on a high-performance precession system produced the true structure in two different ways: 1) by excluding g ¡ 0.25 from the amplitude dataset, and 2) by using the intensities. The two solution methods are complementary, both valid because the thickness of the GITO specimen was within a moderate thickness regime where either method could apply within a pseudo-kinematical interpretation. The experimental results demonstrate that PED has a number of forgiving qualities:

- Zone axis patterns no longer need to be perfectly aligned because the precession angle (large in relation to a mistilt) can compensate for tilt misorientation.
- Pseudo-kinematical interpretation is possible within a large range of thickness.
- Thickness becomes a better-conditioned variable; intensities oscillate more slowly with thickness in general.
- Corrections are not necessary unless the crystal is very thick ('large' thickness).

A wealth of information has been uncovered about the behavior of PED because of multislice's ability to efficiently probe experiment space. First, the validity and robustness of precession multislice was confirmed. Analysis of the error trends over a large range of experimental parameters showed that the behavior of intensities with thickness is predictable. It was confirmed that errors mostly occur for beams near the transmitted beam and encroach into the structure-defining reflections ($\mathbf{g} > 0.25$ Å^{-1}) for moderate to large thickness. For large thickness, correction factors are necessary to combat the low-$\mathbf{g}$ positive offset. Lastly, the thickness range for direct methods has been extended from a few nm to approximately 50 nm for the GITO system.

The systematicity of the errors, in particular the clustering of large errors near the transmitted beam, is highly advantageous because phases for low-index reflections are the easiest ones to extract from high-resolution images. For direct methods codes that predict unknown reflection

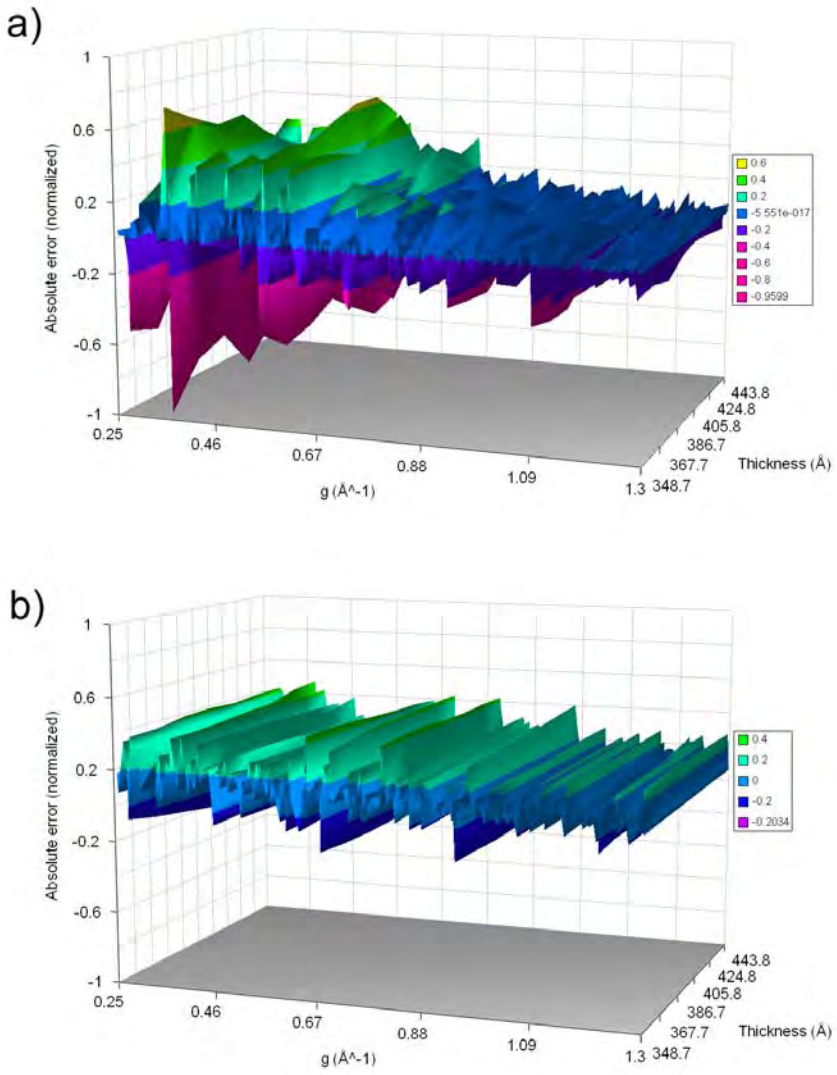

Figure 3.11. 3-D surface plots of absolute amplitude error ($F_{\mathbf{g}}^{exp} - F_{\mathbf{g}}^{kin}$) against $|\mathbf{g}|$ for (a) dynamical and (b) precession data. The ranges of $\mathbf{g}$ and t match experimental parameters from section 3.1. Errors are decreased from (a) to (b) and very little oscillation of intensity occurs with increasing thickness. Granularity of t is 3.17 Å.

intensities (such as fs98) the low-index phases from HREM can be fixed, further enhancing the probability that the direct methods algorithm will find the true structure.

Some other interesting features have been discovered. A critical precession angle exists below which dynamical behavior still dominates. Larger ϕ improves the pseudo-kinematical quality

of the dataset, therefore larger cone semi-angles angles (at least 20-25 mrad) are desirable. As long as HOLZ overlap is avoided and the reflections are uniform enough that they can be easily measured, PED data should be acquired using the largest angle possible on the instrument. Additionally, if the structure is known, precession can be used to pinpoint specimen thickness to 5-10nm accuracy. This final point warrants extra discussion. Some standard methods for determining crystal thickness in the electron microscope are HREM-multislice comparisons, electron energy loss spectroscopy on the zero loss peak, and fringe characterization in convergent beam electron diffraction (O'Keefe and Kilaas 1988; Egerton 1989; Gjønnes and Moodie 1965). These all require structure factors which may not be available when studying novel structures. Precession has an advantage here because it can possibly give the true structure which will serve as the key to unlock the thickness information simultaneously contained within the diffraction data. Keeping in mind the results from this chapter, this is limited to moderate thickness. However, in the next chapter PED's abilities will be extended to include larger thickness.